nature communications

Article

https://doi.org/10.1038/s41467-024-52078-y

Metallic 1T/1T′ phase TMD nanosheets with enhanced chemisorption sites for ultrahigh-efficiency lead removal

Received: 21 March 2024

Accepted: 26 August 2024

Published online: 05 September 2024

Check for updates

Liang Mei[1,14], Mingzi Sun[2,14], Ruijie Yang[1,14], Yaqin Zhang[1], Yuefeng Zhang[1], Zhen Zhang[1], Long Zheng[3], Ye Chen[3], Qinghua Zhang[4], Jiang Zhou[5], Ye Zhu[6], Kenneth M. Y. Leung[7], Wenjun Zhang[1], Jun Fan[1], Bolong Huang[2] ✉, Xiao Cheng Zeng[1], Hyeon Suk Shin[8,9], Chuyang Y. Tang[10], Lin Gu[11] ✉, Damien Voiry[12] & Zhiyuan Zeng[1,13] ✉

Two-dimensional (2D) materials, as adsorbents, have garnered great attention in removing heavy metal ions (HMIs) from drinking water due to their extensive exposed adsorption sites. Nevertheless, there remains a paucity of experimental research to remarkably unlock their adsorption capabilities and fully elucidate their adsorption mechanisms. In this work, exceptional lead ion (Pb^{2+}) (a common HMI) removal capacity (up to 758 mg g^{-1}) is achieved using our synthesized metallic 1T/1T′ phase 2D transition metal dichalcogenide (TMD, including MoS_2, WS_2, TaS_2, and TiS_2) nanosheets, which hold tremendous activated S chemisorption sites. The residual Pb^{2+} concentration can be reduced from 2 mg L^{-1} to 2 μg L^{-1} within 0.5 min, meeting the drinking water standards following World Health Organization guideline (Pb^{2+} concentrations <10 μg L^{-1}). Atomic-scale characterizations and calculations based on density functional theory unveil that Pb^{2+} bond to the top positions of transition metal atoms in a single-atom form through the formation of S-Pb bonds. Point-of-use (POU) devices fabricated by our reported metallic phase MoS_2 nanosheets exhibit treatment capacity of 55 L-water g^{-1}-adsorbent for feed Pb^{2+} concentration of 1 mg L^{-1}, which is 1-3 orders of magnitude higher than other 2D materials and commercial activated carbon.

Heavy metal ions (HMIs) in drinking water poses a grave threat to human health owing to their inherent characteristics of high toxicity, rapid mobility, and non-biodegradability[1–3]. Among the various HMIs, lead ions (Pb^{2+}), cadmium ions (Cd^{2+}), and mercury ions (Hg^{2+}) warrant particular concern due to their well-documented detrimental effects[4,5]. Although, numerous technologies have been applied for removing these ions, including chemical precipitation[6], solvent extraction[7], ion exchange[8], and membrane separation[9–11], their removal efficiency is not sufficient to meet the stringent requirements of extremely low HMI concentrations in drinking water (World Health Organization (WHO) guideline values are 10 μg L^{-1}, 3 μg L^{-1} and 6 μg L^{-1} for Pb^{2+}, Cd^{2+} and Hg^{2+}, respectively)[12].

Adsorption stands out as an effective strategy for the HMIs decontamination from drinking water due to its exceptional uptake capacity, remarkable selectivity, rapid kinetics and simplicity of design and operation[13–15]. According to the hard/soft acid/base (HSAB) theory[9], Lewis soft acids (Pb^{2+}, Cd^{2+}, Hg^{2+}) prefer binding to Lewis soft base groups (compounds containing S, N, or O). Based on this theory, the ideal materials for the adsorption of HMIs should be equipped with rich Lewis soft base groups. Consequently, various materials,

A full list of affiliations appears at the end of the paper. ✉e-mail: bhuang@polyu.edu.hk; lingu@tsinghua.edu.cn; zhiyzeng@cityu.edu.hk

particularly two-dimensional (2D) materials like hexagonal boron nitride (h-BN)[16], graphene oxide (GO)[17], transition metal carbides/nitrides (MXenes)[15], and transition metal dichalcogenides (TMDs)[18], have been developed for HMIs removal.

TMDs, with their unique layered structure and abundant sulfur sites, are promising candidates for HMIs removal. Current research focuses on improving the sulfur atom accessibility of MoS_2 by increasing interlayer spacing[19,20] or exfoliating it into monolayer nanosheets[9]. Phase tuning can also enhance HMIs adsorption, demonstrating higher Pb^{2+} capacity and faster kinetics than the original counterpart[21,22]. Additionally, MoS_2 composites with hydrogels can improve dynamic HMIs processing under continuous flow operations[23]. However, the underlying mechanisms, such as adsorption sites, the morphology of adsorbed Pb^{2+}, and Pb-S bond formation, remain unexplored.

In this work, we developed nearly perfect 2D adsorbents–1T/1T′ TMD nanosheets (MoS_2, WS_2, TaS_2, and TiS_2)–synthesized through electrochemical lithium intercalation based exfoliation method[24,25]. Beneficial from the effective phase tuning (2H to 1T & 1T') and high yield exfoliation (single & bilayer yield >90%), the abundant exposed S chemisorption sites render these nanosheets high adsorption capacity up to 758 mg g^{-1}, rapid adsorption kinetics within 0.5 min, and minimal residual Pb^{2+} concentrations down to 2 μg L^{-1}. The adsorption mechanism and point-of-use (POU) water purification device based on the TMD nanosheets are also elucidated and demonstrated. We elucidated the mechanism of single-atom Pb adsorption through S-Pb bond formation, with Pb adsorbed exclusively on the top transition metal site.

Results and discussion

Ultrahigh-efficiency Pb^{2+} removal

The metallic 1T/1T′ phase TMD nanosheets, including MoS_2, WS_2, TaS_2 and TiS_2, were exfoliated from their bulk counterparts (Supplementary Figs. 1 and 2) via an electrochemical lithium intercalation and exfoliation method (see "Method")[24]. These nanosheets are ultrathin (mono- or bi-layer, high yield than 92%), metallic (1T/1T′ phase), and negatively charged (Supplementary Figs. 3 and 4)[26].

A batch of experiments were conducted to assess the adsorption performances of these exfoliated nanosheets (MoS_2, WS_2, TaS_2, TiS_2) towards various cations, including several toxic transition metal cations (Pb^{2+}, Cu^{2+}, Ni^{2+}, and Zn^{2+}) and some background cations (K^+, Ca^{2+}, Na^+, and Mg^{2+}) (see "Methods" and Supplementary Fig. 5). All of these nanosheets demonstrated nearly 100% removal of Pb^{2+} with initial concentration of 2 mg L^{-1} (Fig. 1a, c, e, g). A high removal efficiency was also demonstrated toward Cu^{2+} (87–90%), but the removal efficiencies for K^+, Ni^{2+}, Na^+, Zn^{2+}, Ca^{2+} and Mg^{2+} were very low (10–50%) (Fig. 1a, c, e, g, Supplementary Tables 1–4 and Supplementary Figs. 6, 7).

To compare the affinity of TMD nanosheets, the distribution coefficients (K_d) for each cation were calculated (see "Methods" and Fig. 1b, d, f, h). The MoS_2, WS_2, TaS_2 and TiS_2 nanosheets exhibited superior K_d values of 5.57×10^7, 3.59×10^7, 3.90×10^7 and 1.58×10^7 mL g^{-1} for Pb^{2+}, respectively, which are 2 to 4 orders of magnitude higher than those for other metal cations (Cu^{2+}, Zn^{2+}, K^+, Ni^{2+}, Na^+, Mg^{2+}, Ca^{2+}), revealing their superior selectivity/affinity toward Pb^{2+}. This is attributed to the tremendous S sites (Lewis soft base groups) in exfoliated TMD nanosheets that can offer strong soft-soft interactions with the Lewis soft acids (Pb^{2+})[9].

Considering the cations of Na^+ and Ca^{2+} are ubiquitous in drinking water, the interference of these cations with high concentration on the adsorption capacities of TMD nanosheets toward Pb^{2+} were further investigated. Results showed that 20 mM $NaNO_3$, 20 mM $Ca(NO_3)_2$, and laboratory tap water have no detectable impact on TMDs' removal efficiency towards Pb^{2+} (Fig. 1i–l).

Further experiments were conducted to reveal the underlying adsorption isotherms and kinetics. As shown in Fig. 1m, the adsorption isotherms of Pb^{2+} on MoS_2, WS_2, TaS_2 and TiS_2 nanosheets can be well fitted with Langmuir model (Supplementary Note 1), indicating monolayer Pb^{2+} adsorption on TMD nanosheets[27]. According to our density functional theory (DFT) calculations, each Pb atom is stabilized by three S atoms through Pb-S bonds (Supplementary Fig. 8), resulting in a maximum stoichiometric Pb/MoS_2 ratio of 3:2 for saturated adsorption. Consequently, the theoretical adsorption capacity of MoS_2 for Pb^{2+} is estimated at 863 mg g^{-1}. Similarly, the calculated theoretical adsorption capacities for WS_2, TaS_2, and TiS_2 are 557 mg g^{-1}, 564 mg g^{-1}, and 1233 mg g^{-1}, respectively. The pH of 6 was chosen to explore the saturated adsorption capacity of MoS_2 for Pb^{2+} while preventing potential interference from hydroxide precipitates under alkaline conditions (Supplementary Note 2). This adjustment significantly boosted the saturated adsorption capacity of Pb^{2+} by MoS_2, yielding an enhanced capacity of 758 mg g^{-1} (Supplementary Fig. 9a). Similarly, Pb^{2+} capacities for WS_2, TaS_2, and TiS_2 increased to 401 mg g^{-1}, 311 mg g^{-1}, and 574 mg g^{-1}, respectively (Supplementary Fig. 9b–d). Consequently, MoS_2, WS_2, TaS_2, and TiS_2 achieved 88%, 72%, 55%, and 47% of their theoretical capacities, respectively. The lower ratios observed for TaS_2 and TiS_2 can be attributed to surface oxidation[28,29], which hinders Pb^{2+} adsorption. MoS_2, although not reaching 100%, may be affected by sulfur vacancies or the slightly acidic pH of 6, since protons have competitive adsorption with Pb^{2+} and thereby reduce the adsorption capacity in comparison with the theoretical value. The kinetic processes for MoS_2, WS_2, TaS_2, and TiS_2 nanosheets in Pb^{2+} adsorption are shown in Fig. 1n. The rapid kinetics of Pb^{2+} adsorption by four TMD nanosheets are evident, with MoS_2 and WS_2 reducing the concentration from 2 mg L^{-1} to 2 μg L^{-1} in just 0.5 and 0.75 min, respectively. While TaS_2 and TiS_2 achieve this reduction to 3 μg L^{-1} in 4 min. This performance aligns perfectly with the stringent WHO guideline value for Pb^{2+} concentrations (10 μg L^{-1}) in drinking water.

Additionally, the stability of Pb^{2+} adsorption on TMD nanosheets was also demonstrated, ensuring that it does not lead to secondary pollution (refer to Supplementary Fig. 10). Upon a comprehensive assessment of MoS_2 in comparison to other representative adsorbents reported in the literatures, we observe that the MoS_2 material developed in this study excels in nearly all aspects (as indicated in Fig. 1o, p and Supplementary Table 5). This superiority includes parameters such as adsorption capacity (q_{max}), distribution coefficient (K_d), removal efficiency (R), adsorption time (t), and the final concentration of Pb^{2+} after adsorption (C_f). The mass production of the MoS_2 nanosheets is easily achieved by scaling up the electrode in our method (see Supplementary Fig. 11). This scalability natures significantly demonstrates their potential in practical application for the removal of Pb^{2+}.

Clarification of Pb^{2+} adsorption sites

The low-magnification transmission electron microscope (TEM) images of TMD-Pb revealed the absence of Pb particles on the nanosheets (Supplementary Fig. 12). The selected area electron diffraction patterns obtained from a flat area of the nanosheets exhibited the (100) and (110) planes of the TMDs (insets in Supplementary Fig. 12), confirming the excellent crystallinity of the TMDs, even after Pb^{2+} adsorption. The scanning electron microscopy (SEM) images coupled with energy-dispersive X-ray (EDX) mapping (see Supplementary Fig. 13) demonstrated the uniform distribution of S, Pb, and transition metal atoms (Mo, W, Ta, and Ti) across the entire nanosheets after Pb^{2+} adsorption.

The high-resolution high-angle annular dark-field scanning transmission electron microscopy (HAADF-STEM) images of TMD-Pb nanosheets displayed the regularly arranged bright dots (Fig. 2a, f, k, p), belonging to the periodic arrangement of the transition metal

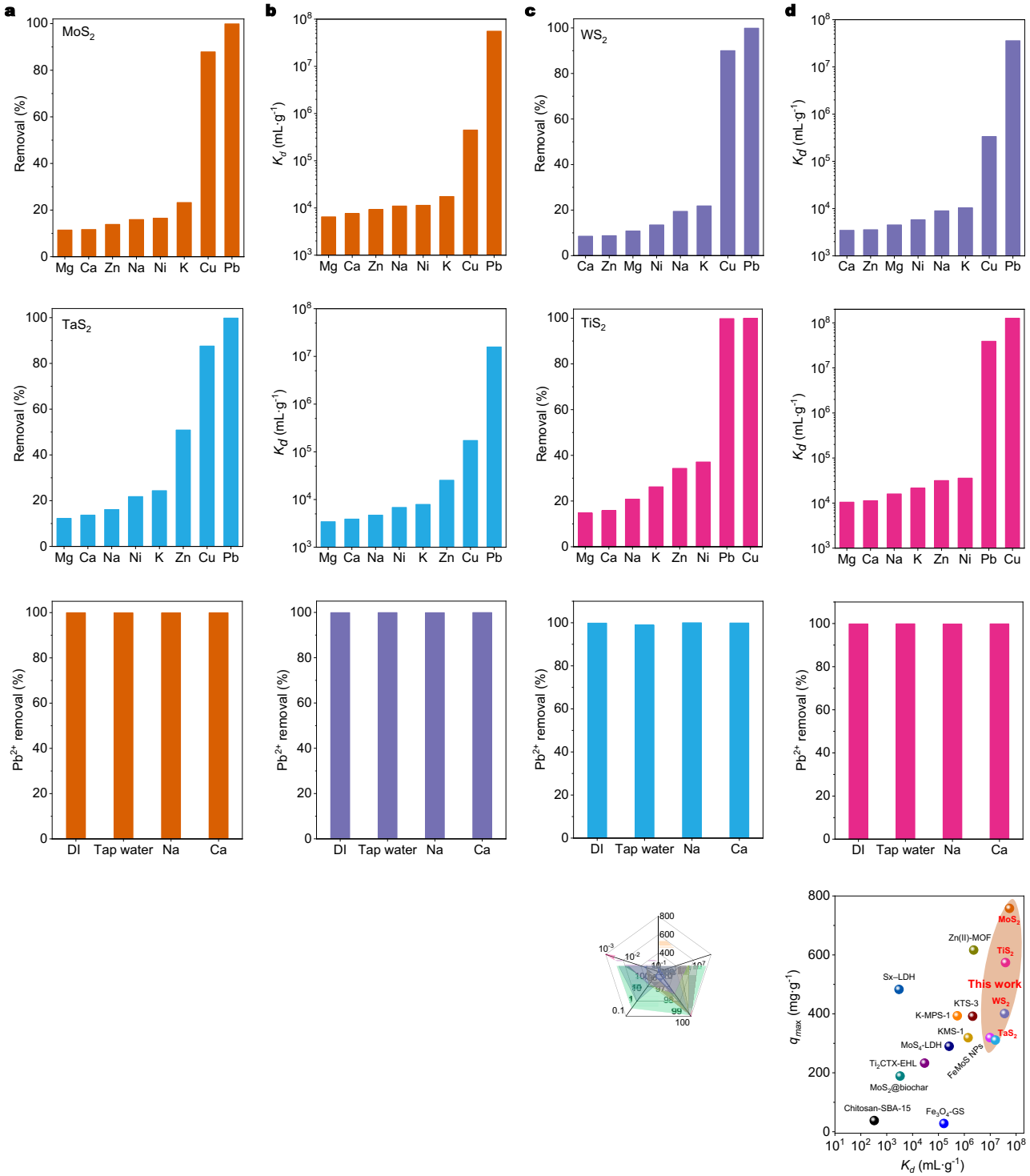

atoms. Clearly, some brighter dots (red circles) also emerged in these images (Fig. 2a, f, k, p and Supplementary Figs. 14–16), belonging to individual Pb atoms[30–32], suggesting the single-atom forms of Pb^{2+} adsorption. Such sing-atom Pb exactly overlap the transition metal atom sites in TMD crystal (Fig. 2b, g, l, q), revealing that the sing-atom Pb are situated on the top sites of transition metal atoms. The HAADF-STEM signal intensity analysis revealed that $d_{Pb\text{-}M} = d_{M\text{-}M}$ (d stands for interatomic distance, M refers to the transition metal atom) (Fig. 2c, h,

https://doi.org/10.1038/s41467-024-52078-y

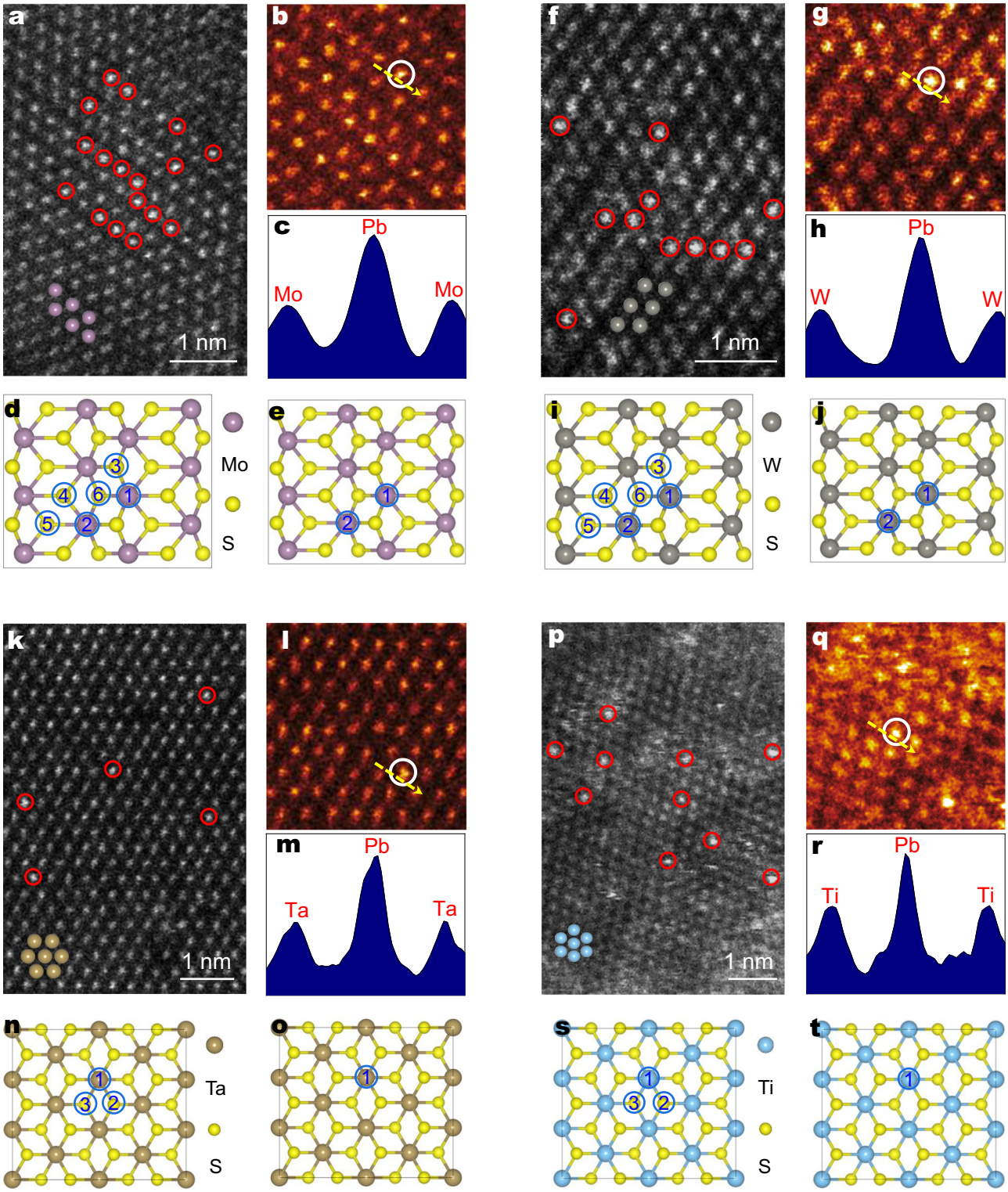

Fig. 2 | HAADF-STEM images of single-atom Pb adsorbed onto single/-bilayer TMD nanosheets. HAADF-STEM images of **a** MoS_2-Pb, **f** WS_2-Pb, **k** TaS_2-Pb, **p** TiS_2-Pb. Insets: the corresponding simulated atomic arrangement model of 1T′-MoS_2, 1T′-WS_2, 1T-TaS_2 and 1T-TiS_2. The brighter dots in red circles represent the single-atom Pb. **b**, **g**, **l**, **q** The corresponding magnified view of STEM images. **c**, **h**, **m**, **r** The intensity profiles along the yellow dots shown in the magnified STEM images. **d**, **e**, **i**, **j**, **n**, **o**, **s**, **t** The initial Pb adsorption sites in each TMD (MoS_2, WS_2, TaS_2, TiS_2) structure and the finally determined adsorption sites through HAADF-STEM results. Encircled numbers mean the different Pb adsorption sites in each TMD structure.

m, r), further indicating that Pb single-atom are precisely overlap transition metal atom sites.

Additionally, the S atoms within the lattice structures of MoS_2-Pb, WS_2-Pb, TaS_2-Pb, and TiS_2-Pb are almost invisible, indicating the formation of octahedral (1T) or distorted octahedral (1T′) phases in the synthesized TMDs[33]. One-dimensional zigzag chains composed of Mo and W atoms were conspicuously observed and consistently appeared throughout the entire HAADF-STEM images (Fig. 2a, f). This distinctive

asymmetric characteristic arises from the presence of the distorted 1T′ structure, thus confirming the exfoliated MoS_2 and WS_2 are 1T′ phases[34,35]. However, this asymmetric structural feature is notably absent in the HAADF-STEM images of both TaS_2-Pb and TiS_2-Pb (Fig. 2k, p), indicating that TaS_2 and TiS_2 adopt a 1T structure[36]. This distinction between 1T′-MoS_2 or WS_2 and 1T-TaS_2 or TiS_2 is further supported by the characteristic peaks observed in the Raman spectra (Supplementary Fig. 17). In principle, the adsorption of Pb^{2+} onto 1T′-MoS_2 or WS_2 offers six distinct types of adsorption sites due to their inherent asymmetric structures (Fig. 2d, i). While 1T-TaS_2 or TiS_2 exhibit symmetrical structures, resulting in a more limited set of three discernible adsorption sites available for Pb^{2+} binding (Fig. 2n, s). Nevertheless, experimental data have conclusively determined that only the top metal (Mo/W/Ta/Ti) sites act as the confirmed adsorption sites for Pb^{2+} binding (Fig. 2e, j, o, t).

To determine whether the adsorption of Pb^{2+} by MoS_2, WS_2, TaS_2, and TiS_2 is a physical or chemical process, we conducted synchrotron-based X-ray absorption fine structure (XAFS) measurements. The normalized X-ray absorption near-edge structure (XANES) spectra of the Pb L_3-edge for TMD-Pb samples closely resemble those of PbO or PbS (Fig. 3a), indicating that the average oxidation state of Pb species is approximately 2, and the primary form of existence Pb atoms is single-atom form (because the oxidation state of Pb species in the form of Pb particles or clusters is expected to be zero)[37–39]. Further insights into the chemical bonding were obtained through *R*-space curves (Fig. 3b) derived from the extended X-ray absorption fine structure (EXAFS) spectra of the Pb L_3-edge, revealing the presence of Pb-S bonds in TMD-Pb samples, which is consistent with the standard PbS. No discernible peak corresponding to Pb-Pb bonds, like the peak observed in Pb foil, further confirms the formation of single-atom Pb. Additionally, no peaks related to Pb compounds were detected in the XRD spectra of TMD-Pb samples (Fig. 3c), further illustrating an atomic dispersion of Pb in TMD crystal lattice with the crystalline domains below the detection limit of XRD. A similar phenomenon, where no metallic particles could be detected, was also observed for other metal cations adsorbed on TMD nanosheets, even after saturation of adsorption (see Supplementary Fig. 18).

Due to its powerful resolution in both *k* and *R* spaces, wavelet transform (WT)-EXAFS analysis was applied to investigate the atomic configuration of TMD-Pb[40]. Pb foil exhibited the maximum intensity of Pb-Pb signals in *R*-space at $R = 3.5$ Å and Pb-Pb signals in *k*-space at $k = 7.5$ $Å^{-1}$ (Supplementary Fig. 19a). PbO displayed resolved spectra of Pb-O signals in *R*-space at $R = 1.7$ Å and Pb-O signals in *k*-space at $k = 8.0$ $Å^{-1}$ (Supplementary Fig. 19b). In contrast, the WT contour plots of MoS_2-Pb, WS_2-Pb, TaS_2-Pb, and TiS_2-Pb (Fig. 3d–g) reveal a single intensity maximum at around $R = 2.3$ Å and *k*-space of 6.0–8.0 $Å^{-1}$, exclusively assigned to the Pb-S contribution. This analysis unequivocally confirms the absence of Pb-Pb bonds, indicating that no Pb clusters or particles are formed in TMD-Pb. This aligns perfectly with the findings from HAADF-STEM and XRD results, providing strong evidence for the atomically dispersed nature of Pb after adsorption on TMD structures. Moreover, these atomically dispersed Pb ions are bound to the S atoms of TMDs, forming stable S-Pb bonds that help stabilize the adsorption configuration. Consequently, these experimental findings strongly support the conclusion that Pb^{2+} adsorption on TMDs represents a form of chemical adsorption, with the S atoms of TMDs serving as the primary adsorption sites. Further evidence for chemical adsorption is drawn from the adsorption kinetics of Pb^{2+} by single/bi-layer TMD nanosheets (Supplementary Fig. 20). The excellent fit of the data to the pseudo-second-order kinetic model provides compelling evidence that the chemisorption process governs the rate-determining step in the adsorption process (Supplementary Note 3)[5]. To deepen our understanding of the interaction between Pb^{2+} and TMDs, we conducted X-ray photoelectron spectroscopy (XPS) on both pristine $Pb(NO_3)_2$ and Pb^{2+} adsorbed onto the TMDs. The emergence of a new peak at a binding energy of 141.0 eV was attributed to Pb 4*f* (Supplementary Fig. 21), confirming the successful adsorption of Pb^{2+} onto MoS_2, WS_2, TaS_2, TiS_2. In the high-resolution spectra of Pb 4*f* depicted in Fig. 3h, it is observed that the peaks corresponding to Pb $4f_{7/2}$ and $4f_{5/2}$ in TMD-Pb have shifted to lower binding energies (138.6 and 143.5 eV, respectively) compared to those of $Pb(NO_3)_2$ (139.5 and 144.3 eV, respectively). This shift suggests a strong interaction between TMDs and Pb^{2+}, with TMDs transferring electrons to Pb^{2+}[27]. Therefore, the peaks attributed to Mo$3d_{5/2\text{-}3/2}$, W$4f_{7/2\text{-}5/2}$, Ta$4f_{7/2\text{-}5/2}$ and Ti$2p_{3/2\text{-}1/2}$, as well as the corresponding S$2p_{3/2\text{-}1/2}$ peaks, all shifted to higher binding energies after Pb^{2+} adsorption (Fig. 3i–l and Supplementary Fig. 22).

DFT calculations

We further apply the DFT calculations to investigate the corresponding adsorption behaviors for Pb^{2+} on different TMD surfaces regarding both thermodynamic trends and electronic structures. For four types of TMD materials, we have compared the adsorption energies of different metal ions on TMD surfaces based on the most stable configurations (Fig. 4a–d). For 1T′-MoS_2 and 1T′-WS_2, there are 6 possible adsorption sites while 1T-TaS_2 and 1T-TiS_2 have 3 different adsorption sites due to the higher symmetrical level of lattice structures (Supplementary Fig. 23). For most of the surfaces, we have demonstrated that Pb^{2+} are much more preferred to adsorb on the TMD surface than other metal ions due to the much lower adsorption energies. There is only one exception, where Cu^{2+} display a slightly stronger adsorption trend than Pb^{2+} on 1T-TiS_2. These different adsorption energies highly agree well with their removal efficiency (Fig. 1a, c, e, g). The stronger adsorption strengths of the Pb^{2+} benefit the further removal of the Pb^{2+} from the solution. Among different TMD surfaces, the adsorption trends of Pb^{2+} show an order of 1T′-MoS_2 > 1T-TiS_2 > 1T′-WS_2 > 1T-TaS_2, which is supportive of the removal efficiency of different TMDs (Fig. 1m). Then, we further compare the adsorption energies of Pb^{2+} on different possible sites on the surface based on the structures. For both 1T′-MoS_2 and 1T′-WS_2, it is noted that the Mo-top and W-top sites supply the most stable configurations (Fig. 4e, f). From adsorption site 1 to 6, the adsorption energies and the average Pb-S bond lengths exhibit a converse trend, in which the S-top sites with the longest Pb-S bond lengths are the most energetically unfavored adsorption sites. For 1T′-MoS_2, the S-top sites are meta-stable sites, where the Pb^{2+} is easy to migrate to the nearby stable Mo-top sites driven by the much stronger adsorption trends with largely reduced energy (-1.5 eV). A similar phenomenon is also revealed on 1T′-WS_2, where the W-top sites become an energy well, resulting in the stabilizations of Pb^{2+} from nearby meta-stable sites. It is worth mentioning that the most stable adsorption configurations of Pb^{2+} slightly deviate from the Mo-top sites, which is attributed to the reduced symmetrical level of the nearby S sites (Supplementary Figs. 24 and 25). Meanwhile, for 1T-TaS_2 and 1T-TiS_2, we discover that the three possible adsorption sites also exhibit the opposite trend between the adsorption energies and the Pb-S bond lengths (Fig. 4g, h). The metal-top sites still display the dominant advantages as the most stable adsorption configurations with the lowest adsorption energies. For Pb^{2+} adsorbed on metal-top sites, the migrations to nearby S-top sites are very difficult, which need to overcome an energy barrier of 1.51 eV and 1.01 eV for 1T-TaS_2 and 1T-TiS_2, respectively. In addition, we notice that the metal-top adsorptions are highly stable without deviations due to the higher symmetrical level of lattice, resulting in slightly decreased Pb-S bond lengths than that of 1T′-MoS_2 and 1T′-WS_2 (Supplementary Fig. 26). These energy favorable M-top sites (M = Mo, W, Ta, Ti) in 4 TMDs for Pb^{2+} adsorption are highly consistent with the HAADF-STEM results (Fig. 2).

To further reveal the electronic interactions between Pb^{2+} and TMD surfaces, we have compared the projected partial density of states

https://doi.org/10.1038/s41467-024-52078-y

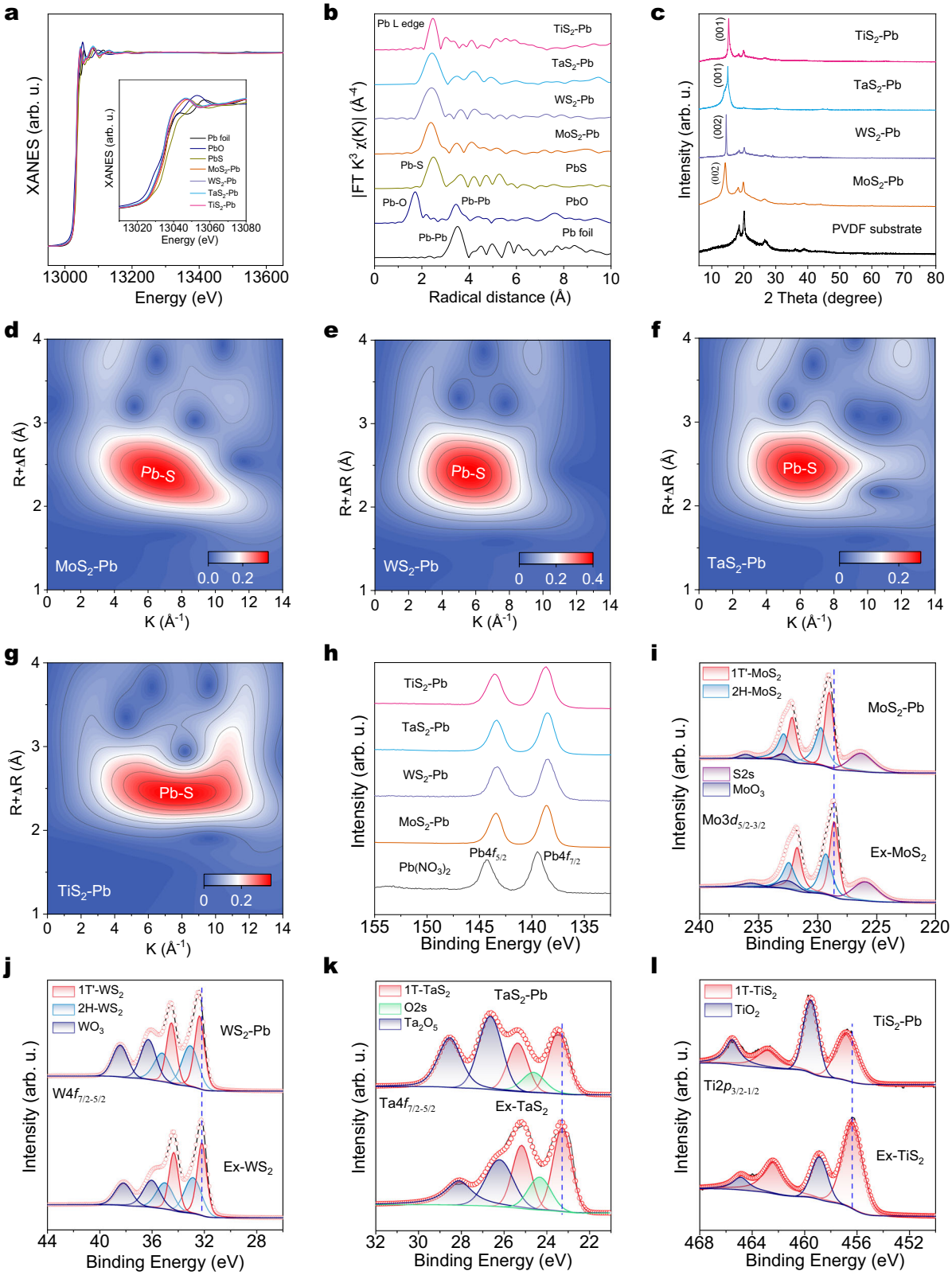

Fig. 3 | Chemisorption via forming Pb-S bond. a Normalized X-ray absorption near-edge structure (XANES) spectra at the Pb L_3-edge of Pb foil, PbO, PbS, MoS_2-Pb, WS_2-Pb, TaS_2-Pb and TiS_2-Pb. Inset shows the enlarged detail for the range of 13,010–13,080 eV. **b** Corresponding extended X-ray absorption fine structure (EXAFS) spectra. FT Fourier-transformed. **c** XRD patterns of MoS_2-Pb, WS_2-Pb, TaS_2-Pb and TiS_2-Pb that collected onto the PVDF substrate. **d**–**g** Wavelet-transform images of MoS_2-Pb, WS_2-Pb, TaS_2-Pb and TiS_2-Pb at Pb L_3 edge. *R* denotes radical distance. Inset in each figure show the gradient scale. **h** XPS Pb 4*f* spectra of MoS_2-Pb, WS_2-Pb, TaS_2-Pb, TiS_2-Pb and $Pb(NO_3)_2$. **i**–**l** XPS Mo3*d*, W4*f*, Ta4*f*, Ti2*p* for pristine exfoliated TMD nanosheets and after Pb^{2+} adsorption. Ex represents exfoliated, "arb. u." denotes arbitrary units.

https://doi.org/10.1038/s41467-024-52078-y

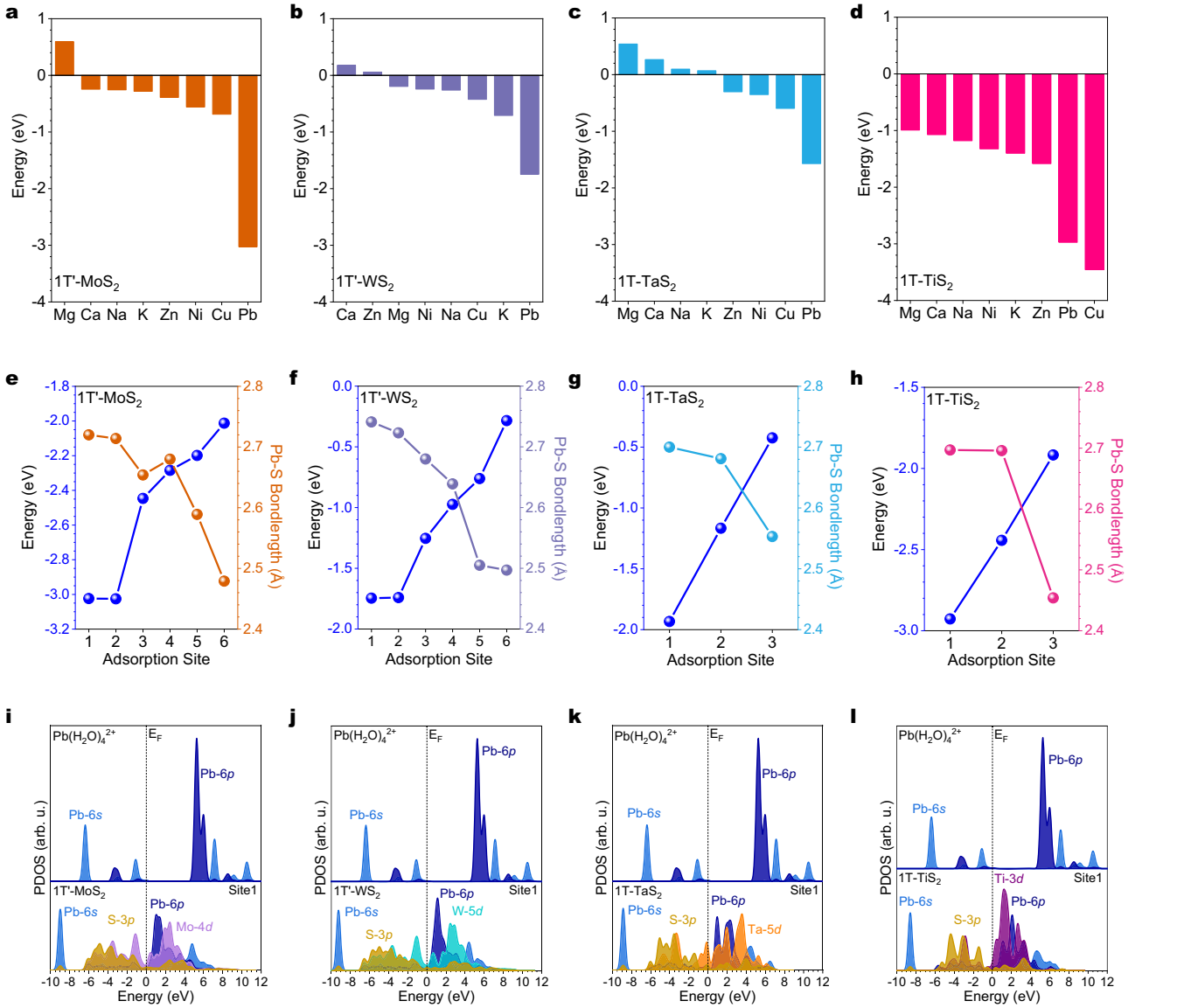

Fig. 4 | Adsorption mechanisms of Pb^{2+} on 1T/1T′ TMDs revealed by DFT calculations. The adsorption energies of different metal ions on **a** 1T′-MoS_2, **b** 1T′-WS_2, **c** 1T-TaS_2, and **d** 1T-TiS_2. The comparisons of adsorption energies and Pb-S average bond lengths for different adsorption sites on **e** 1T′-MoS_2, **f** 1T′-WS_2, **g** 1T-TaS_2, and **h** 1T-TiS_2. The PDOS of comparisons for Pb adsorptions on **i** 1T′-MoS_2 (Mo-4*d*, S-3*p* represent the 4*d* and 3*p* orbitals of 1T′-MoS_2, Site1 corresponds to Pb adsorption site shown in Fig. 2d), **j** 1T′-WS_2 (W-5*d*, S-3*p* represent the 5*d* and 3*p* orbitals of 1T′-WS_2, Site1 corresponds to Pb adsorption site shown in Fig. 2i), **k** 1T-TaS_2 (Ta-5*d*, S-3*p* represent the 5*d* and 3*p* orbitals of 1T-TaS_2, Site1 corresponds to Pb adsorption site shown in Fig. 2n), and **l** 1T-TiS_2 (Ti-3*d*, S-3*p* represent the 3*d* and 3*p* orbitals of 1T-TiS_2, Site1 corresponds to Pb adsorption site shown in Fig. 2s). $Pb(H_2O)_4^{2+}$ represents hydrated lead ion, E_F denotes Fermi level, Pb-6*s* and Pb-6*p* represent the 6*s* and 6*p* orbitals of $Pb(H_2O)_4^{2+}$. "arb. u." denotes arbitrary units.

(PDOS) before and after adsorptions of Pb^{2+} on the most stable metal-top sites (Site 1) (Fig. 4i–l). For $Pb(H_2O)_4^{2+}$, it is noted that the dominant peak of Pb orbitals locate far above the Fermi level (E_F). After the adsorption on TMD surfaces, the corresponding *s*, *p* orbitals have evidently downshifted towards the E_F, which is induced by the strong electron transfer from TMDs. For all the TMD surfaces, we notice the good matching between S-3*p* orbitals and Pb-6*s* orbitals, which proves the formation of Pb-S bonds due to the chemisorption (Supplementary Fig. 8), align well with XAS results (Fig. 3d–g). Moreover, the *p*-*p* orbital overlapping between Pb and S sites is also observed, supporting the efficient electron transfer. The efficient *s*-*p* and *p*-*p* coupling guarantees stable Pb-S bond formation. In contrast, the main peak positions of *d* orbitals of Mo, W, Ta, and Ti show obvious mismatch with *s*, *p* orbitals of Pb sites, which suppress the electron transfer as well as bonding formation, leading to the preferences for Pb-S bond formation.

Portable point-of-use (POU) device

The regeneration of TMDs after Pb^{2+} adsorption can be achieved by employing potent chelating agents to bind with Pb^{2+}. In this study, we chose ethylenediaminetetraacetic acid (EDTA) to regenerate MoS_2. Following treatment of the MoS_2-Pb sample with EDTA, XPS results displayed a significant reduction in the Pb signal (Fig. 5a). Even after five regeneration cycles, MoS_2 maintained a Pb^{2+} removal efficiency of approximately 94% (Fig. 5b). The slight decrease in removal efficiency after regeneration could be attributed to factors such as aggregation or partial oxidation of the MoS_2 nanosheets[9].

The capacity, selectivity, and regenerability are crucial criteria when considering single-layer TMD nanosheets as potential components for developing a portable POU filter for Pb^{2+} removal from contaminated water. Such a filter should also possess attributes like flexibility, user-friendliness, and cost-effectiveness[41]. To demonstrate

https://doi.org/10.1038/s41467-024-52078-y

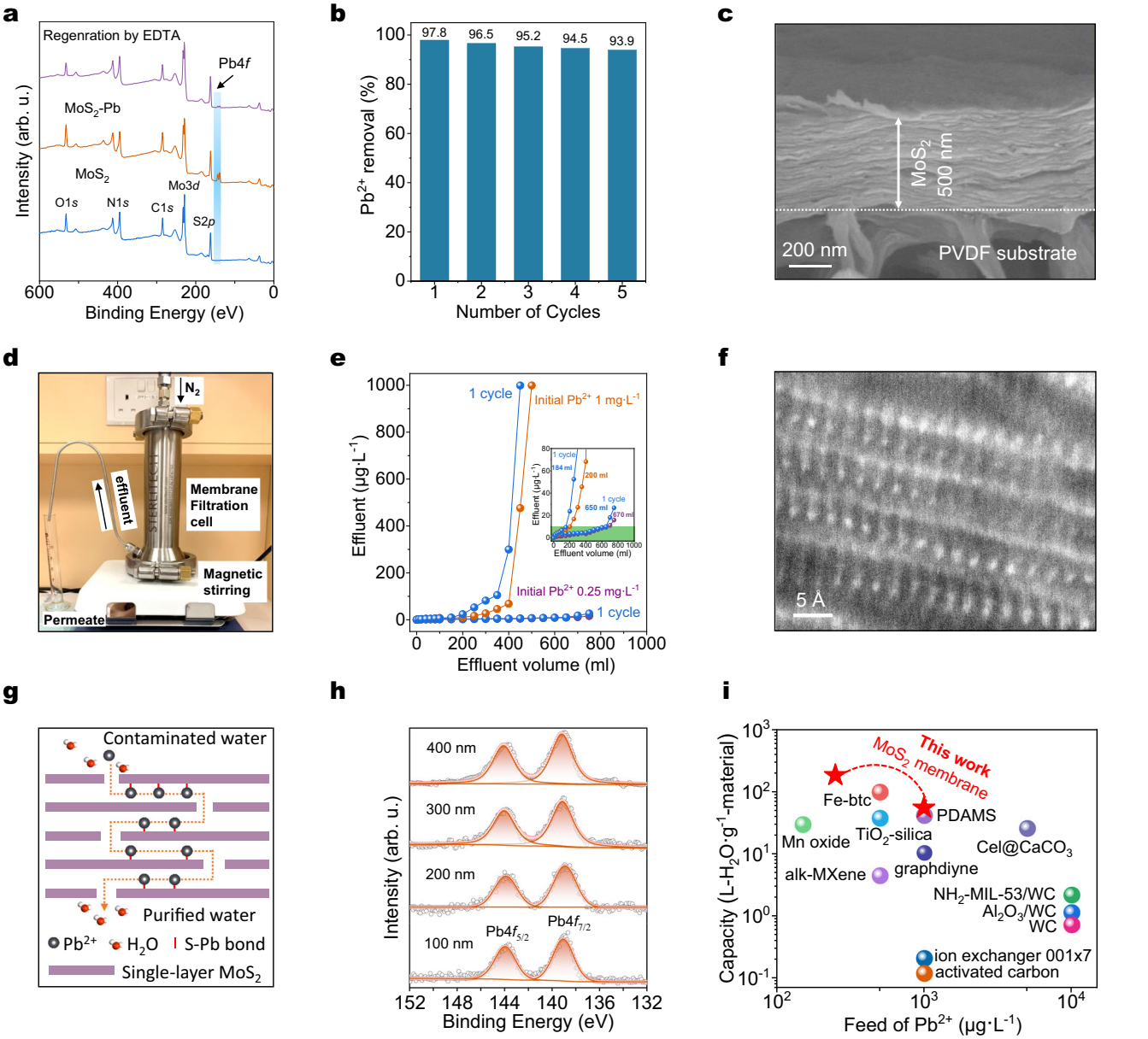

Fig. 5 | Regeneration and membrane filtration performance. a Overall XPS full scanning spectra of MoS_2-Pb regenerated by EDTA. "arb. u." denotes arbitrary units. **b** Regeneration performance of MoS_2 for Pb^{2+} removal was evaluated at an initial Pb^{2+} concentration of 2 mg L^{-1}, pH of 5, and room temperature. **c** Cross-sectional SEM image of MoS_2 membrane. PVDF polyvinylidene difluoride. **d** Schematic of the pressure assisted Pb^{2+} filtration experiment through MoS_2 membrane. **e** Performance of MoS_2 membranes for filtering a feedwater containing 0.25 and 1 mg L^{-1} Pb^{2+}, respectively. The treatment capacity is defined as the total effluent volume at the breakthrough point, which was reached when the effluent Pb^{2+} concentration reached 10 μg L^{-1}. Inset shows the enlarged detail for the effluent concentration range of 0–80 μg L^{-1}, with the green region indicating effluent Pb^{2+} concentrations below 10 μg L^{-1}. **f** Cross-sectional HAADF-STEM image of MoS_2 membrane after Pb^{2+} filtration experiment. **g** Schematic of the single-atom lead adsorbed into the nanochannel of laminate MoS_2 membrane. **h** XPS depth profile of the MoS_2 membrane after filtering Pb^{2+} solution. **i** Comparison of the treatment capacities (L-water g^{-1}-material) of MoS_2 membrane and other adsorptive membranes reported in the literatures. The details can be found in Supplementary Table 6.

their capability, we selected MoS_2 due to its superior adsorption capacity and strong affinity for removing Pb^{2+} compared to other TMD nanosheets. Subsequently, we fabricated a MoS_2 lamellar membrane through vacuum filtration of the TMD nanosheets solution on a porous substrate ("Methods"). As depicted in Fig. 5c, the layer-by-layer structure of the MoS_2 membrane is clearly visible in the SEM cross-sectional image, with a membrane thickness of approximately 500 nm. Following this, we conducted pressure-assisted filtration experiments on the MoS_2 membrane ("Methods" and Fig. 5d) using feed water with varying Pb^{2+} concentrations from 0.25 to 1 mg L^{-1}. Due to the inherent limitations of MoS_2 in its adsorption capacity for Pb^{2+}, a breakthrough point is reached once adsorption saturation is achieved. As demonstrated in Fig. 5e, when subjected to a feed concentration of 1 mg L^{-1} Pb^{2+}, the effluent volume can reach up to 200 ml before the Pb^{2+} concentration exceeds 10 μg L^{-1}, which is the WHO guideline value for Pb^{2+} concentration in drinking water[12]. Additionally, the water flux was measured at approximately 5 L m^{-2} h^{-1} bar^{-1} (Supplementary Fig. 27). By reducing the feed concentration of Pb^{2+} to 0.25 mg L^{-1}, the effluent volume can be further increased to 670 ml. Moreover, the MoS_2 membrane was regenerated after reaching saturation with Pb^{2+} by flushing it with EDTA solution. Following EDTA cleaning, a second filtration cycle was conducted, and the regenerated MoS_2 membrane

was still able to reduce the Pb^{2+} concentration from 1 mg L^{-1} to less than 10 µg L^{-1}. It exhibited a treatment volume of 184 mL, which is equivalent to 92% of the original value of a fresh MoS_2 membrane (200 ml). Furthermore, the recovery rate was 97% when decreasing the Pb^{2+} concentration from 0.25 mg L^{-1} to below 10 µg L^{-1} (650 ml vs 670 ml). These high recovery rates confirmed the excellent reusability of the MoS_2 membrane for Pb^{2+} filtration. After adsorption, the MoS_2 membrane was characterized by cross-sectional HAADF-STEM image as shown in Fig. 5f, which reveals the presence of single-atom Pb that identifies as brighter spots within the 2D nanochannel of the MoS_2 membrane (Fig. 5g). These Pb atoms are adsorbed on the top Mo sites, consistent with the HAADF-STEM image of depicting Pb^{2+} adsorption on 2D MoS_2 nanosheets (Fig. 2a). Furthermore, the predominant mechanism for Pb^{2+} removal, which involves Pb^{2+} adsorption into the 2D nanochannel rather than membrane rejection[9], was reaffirmed through XPS etch measurements along the membrane stacking direction. As shown in Fig. 5h and Supplementary Fig. 28, noticeable Pb 4*f* intensity was observed at all depths (100–400 nm) of the MoS_2 membrane rather than only on the surface layers. The treatment capacity of the adsorptive membrane was determined by the total effluent volume at the breakthrough point. When compared with other reported adsorptive membranes (MXene[18], graphdiyne[29], activated carbon[28], ion exchanger[28]), our developed MoS_2 membrane exhibited a treatment capacity that was 1-3 orders of magnitude higher. This remarkable performance surpassed most other adsorptive membranes, including commercial ones (Fig. 5i and Supplementary Table 6). This exceptional performance can be attributed to the high adsorption capacity and selectivity of MoS_2 for Pb^{2+}, as well as the full accessibility of S atoms within the 2D nanochannel for binding with Pb^{2+}.

Additionally, the stability of the MoS_2 membrane in aqueous environment is noteworthy. After immersing it in water for a month, there is no apparent loosening of the membrane or detachment from the substrate (Supplementary Fig. 29a). This stability aligns with previous findings that the robust Van der Waals forces between MoS_2 nanosheets can effectively prevent the layered MoS_2 nanosheets from delaminating in water[42]. Similar membrane stability in deionized water was also observed for WS_2, TaS_2, and TiS_2 (Supplementary Fig. 29b–d). Finally, four TMD membranes were soaked in aqueous solutions with pH values ranging from 0 to 14 for 3 days, no significant differences on XRD spectra were observed between the pristine MoS_2/WS_2/TaS_2/TiS_2 membranes and after 72 h of soaking (Supplementary Fig. 30), suggesting a well-maintained lamellar configuration, demonstrating their stable lamellar structure for membrane-based filtration applications under varying pH conditions.

Based on our comprehensive characterizations in combination with theoretical calculation, Fig. 6 illustrates the successful high-yield preparation of single/bi-layer TMD nanosheets featuring metallic 1T/1T′ phases, and highlights their outstanding performance for the Pb^{2+} removal application. Here is a breakdown of the key factors contributing to this success, as summarized in Fig. 6a: 1) Precise lithium ion (Li^+) intercalation: The electrochemical lithium intercalation and exfoliation method was employed with precise control over the amount of Li^+ intercalated. This approach ensured the optimal exfoliation conditions, resulting in the highest yield of single/bi-layer TMD (≥92%). This maximized the exposure of the in-plane S atoms within the TMD bulk, creating an abundance of Pb^{2+} adsorption sites and ultimately leading to a high adsorption capacity. 2) Electron transfer induced phase change: The controlled electron transfer from intercalated lithium atoms to the layered TMD materials induced significant phase changes, transitioning from the 2H phase to the 1T′ phase. This phase change facilitated the uniform distribution of additional electrons or negative charges on the S sites of the metallic phase TMD nanosheets. These charged sites attracted positively charged Pb^{2+}, forming strong S-Pb bonds at the top metal sites, thereby achieving rapid Pb^{2+} adsorption kinetics. 3) Efficient adsorption sites: The combination of abundant and activated (due to extra electron doping) S adsorption sites resulted in minimal residual concentrations of Pb^{2+} after the adsorption process. For the adsorption sites identification, theoretical calculations elucidated that metallic 1T′ phase MoS_2 or WS_2 possessed six stable adsorption sites, labeled as S1 (M-top), S2 (M-top), S3 (S-top), S4 (S-top), S5 (S-hollow) and S6 (S-hollow), while 1T-TaS_2 and 1T-TiS_2 possessed three stable adsorption sites, labeled as S1 (M-top), S2 (S-top), S3 (S-hollow). Among these, only the adsorption sites-S1 (M-top) and S2 (M-top) for 1T′ phase MoS_2 or WS_2, as well as S1 (M-top) for 1T phase TaS_2 or TiS_2 with the lowest adsorption energies, were capable of accommodating Pb^{2+} for adsorption. This finding aligns with our observations through HAADF-STEM, as depicted in Fig. 6b. Therefore, compared to other TMDs studied for Pb^{2+} adsorption (Supplementary Table 7), our work not only achieves remarkable adsorption performance-such as a capacity of up to 758 mg g^{-1}, rapid kinetics as fast as 0.5 min, and minimal residual content as low as 2 µg L^{-1}, but also elucidates the mechanism of single-atom Pb adsorption exclusively on the top transition metal sites through the formation of S-Pb bonds with TMDs.

In summary, our study presents a significant advancement in the efficient removal of Pb^{2+} through the development of a series of metallic 1T/1T′ phase TMD nanosheets, including MoS_2, WS_2, TaS_2, and TiS_2, all characterized by a high yield of single/bi-layer structures with tremendous activated S chemisorption sites. Our achievements encompass rapid adsorption kinetics, minimal residual content, high adsorption capacity, exceptional selectivity, and unparalleled removal efficiency, surpassing previously reported Pb^{2+} adsorbents. Through a combination of comprehensive multimodal characterizations and rigorous theoretical calculations, these exceptional Pb^{2+} removal performances are attributed to the activation of surface S chemisorptive sites on TMD nanosheets, facilitated by electron doping during Li^+ intercalation. The single-atom form with the formation of S-Pb bonds by Pb^{2+} adsorption mechanism is proposed and proven. Furthermore, our work extends its implications by demonstrating the potential application of MoS_2 membranes as highly effective POU filters for Pb^{2+} removal. These findings underscore the remarkable potential of metallic 1T/1T′ phase TMD nanosheets for mitigating heavy metal contamination in drinking water to align with WHO guideline values. The determined adsorption mechanism might be used to improve the HMI adsorption performance via tuning the microenvironment of the adsorption sites.

Methods

Materials

Molybdenum disulfide (MoS_2, Innochem), Tungsten disulfide (WS_2, Macklin), Tantalum disulfide (TaS_2, Sixcarbon Technology), Titanium disulfide (TiS_2, Sigma-Aldrich), N-methylpyrrolidone (NMP, Aladdin), Polyvinylidene difluoride (PVDF, Sigma-Aldrich), Natural graphite (Bay Carbon), Copper foil (Aritech Chemazone Private), Lithium foil (DodoChem), Polypropylene (pp) film (Celgard 2300), Lithium hexafluorophosphate dissolved in ethylene carbonate, dimethyl carbonate and methylene carbonate mixture (1 M $LiPF_6$ in EC:DMC:EMC, 1:1:1 vol.%, DodoChem), Lead sulfide (PbS, 99.995%, Aladdin), Lead (II) nitrate ($Pb(NO_3)_2$, ≥99.0%, Fisher chemical), Copper nitrate trihydrate ($Cu(NO_3)_2.3H_2O$, AR, Aladdin), Cadmium nitrate tetrahydrate ($Cd(NO_3)_2.4H_2O$, Aladdin), Potassium nitrate (KNO_3, ≥99.0%, Aladdin), Sodium nitrate ($NaNO_3$, ≥99.0%, VWR Chemicals), Nickel(II) nitrate hexahydrate ($Ni(NO_3)_2.6H_2O$, Duksan Pure Chemicals), Zinc nitrate hexahydrate ($Zn(NO_3)_2.6H_2O$, 98%, Alfa Aesar), Calcium nitrate tetrahydrate ($Ca(NO_3)_2.4H_2O$, ≥97%, Alfa Aesar), Magnesium nitrate hexahydrate ($Mg(NO_3)_2.6H_2O$, Alfa Aesar). Ethylenediaminetetraacetic acid (EDTA, Aladdin), Nitric acid (HNO_3, 69%, VWR Chemicals),

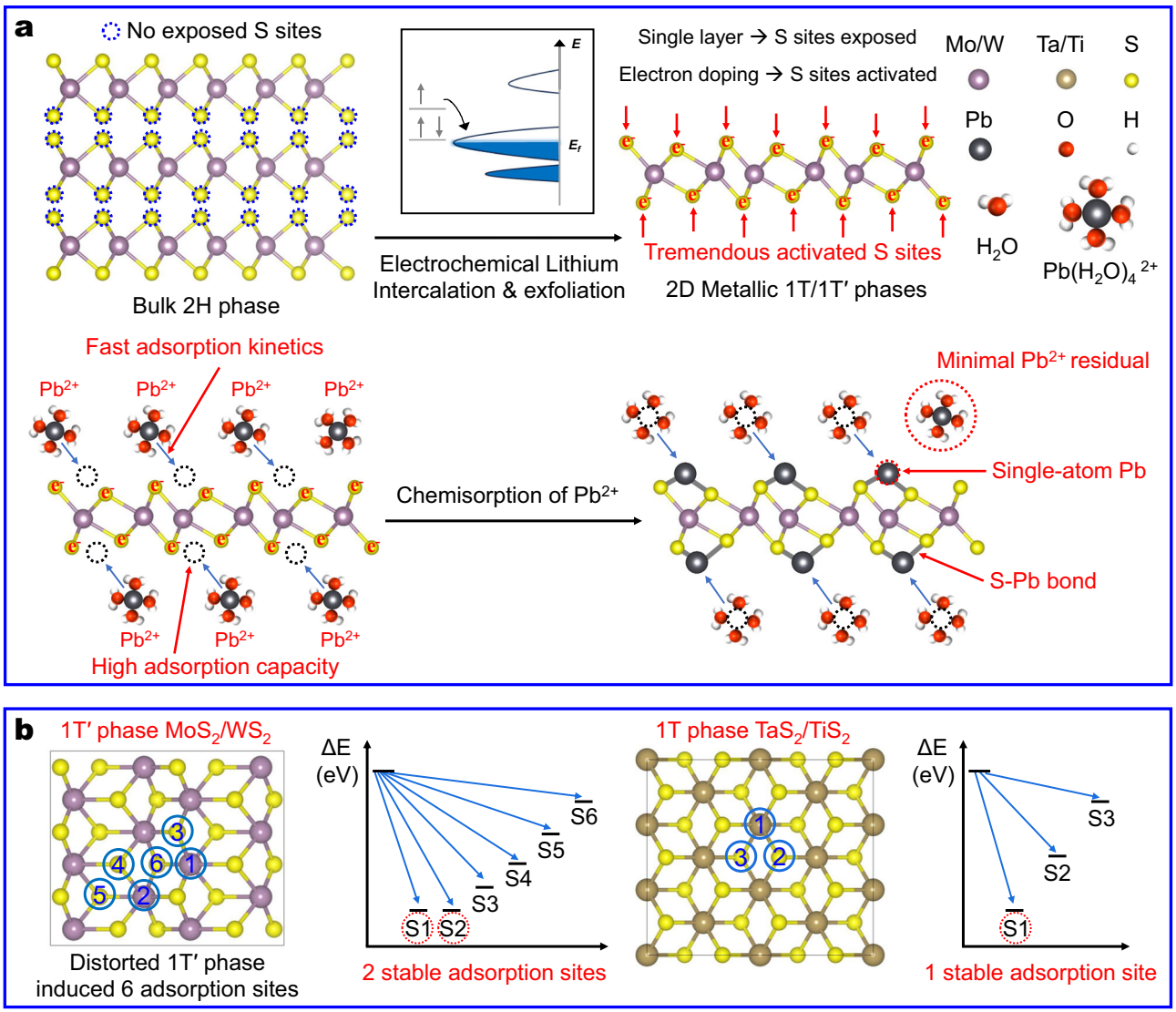

Fig. 6 | Schematic illustration of metallic 1T/1T′ phase TMD nanosheets for ultrahigh-efficiency lead removal. a Through optimizing electrochemical lithium intercalation and exfoliation method, we synthesized a serial of 1T/1T′ TMD nanosheets with high single/bi-layer yields, that tremendous S sites were exposed and activated through electron doping and phase transformation, which contributed to TMD′ superior Pb^{2+} removal performances in the form of high adsorption capacity, fast adsorption kinetics and minimal Pb^{2+} residual. E denotes energy, and E_f represents fermi level. **b** 1T′ phase MoS_2 or WS_2 possess two stable adsorption sites: S1 (M-top) and S2 (M-top), while 1T phase TaS_2 or TiS_2 only show one stable adsorption site: S1 (M-top).

Hydrogen peroxide (H_2O_2, 30%, Anaqua global international Inc. Limited), Acetone (CH_3COCH_3, 99.5%, Anaqua global international Inc. Limited). The Milli-Q water (Millipore, Billerica, MA) was used in all experiments.

Synthesis of single/bi-layer TMD nanosheets (MoS_2, WS_2, TaS_2, TiS_2)

MoS_2, WS_2, TaS_2, and TiS_2 nanosheets were prepared using an electrochemical lithium intercalation-based exfoliation method (Supplementary Fig. 3a). The process commenced with the intercalation of Li^+ into the interlayer spaces of bulk TMDs (4 mg), achieved through the application of galvanostatic discharge conditions on a coin cell. The current and cutoff voltage are set as follows: 0.05 mA and 0.9 V for MoS_2; 0.025 mA and 0.9 V for TaS_2 and TiS_2; 0.08 mA and 0.7 V for WS_2. Following the intercalation step, exfoliation was performed by subjecting the lithiated TMD samples to sonication in DI water (10 ml). The introduction of Li^+ into the interlayer spacing resulted in an expansion of the interlayer gaps, thereby weakening the van der Waals forces that bound the layers together. Concurrently, the generation of hydrogen gas during sonication further enhanced the efficiency of exfoliation, typically completing within a few minutes (5-10 min). The exfoliated TMD nanosheets were subsequently purified through multiple rinses with DI water. Please handle the unreacted lithium foil with care after disassembling the coin cell.

Synthesis of the TMD membranes

The purified TMD nanosheets were redispersed in DI water, and subsequently vacuum-filtrated onto a porous polymer substrate (PVDF, 220 nm pore size, 25 mm in diameter) to fabricate the TMD membrane[43]. The thickness of the membrane was precisely tuned by controlling the volume of the filtrated solution.

Adsorption of metal cations by TMD nanosheets

In this study, batch experiments were conducted to investigate the adsorption of various metal cations onto TMD nanosheets (MoS_2, WS_2, TaS_2, and TiS_2). Nine different metal cations, including Pb^{2+}, Cu^{2+}, Cd^{2+},

K^+, Ni^{2+}, Na^+, Zn^{2+}, Ca^{2+}, and Mg^{2+}, were evaluated in the form of nitrate salts to eliminate any potential interference from anions. The procedure involved mixing the TMD nanosheets solution with each individual metal cation at a concentration of 2 mg L^{-1}, followed by 12 h of stirring. After this incubation period, the TMD nanosheets with adsorbed cations were separated using 0.22 µm PVDF syringe filters, and the remaining cation concentration in the filtrate solution was determined using Inductively coupled plasma optical emission spectroscopy (ICP-OES) or Inductively Coupled Plasma Mass Spectrometer (ICP-MS) (Supplementary Fig. 5). The removal rate (R) was calculated using the following equation:

$$R = [(C_0 - C_f)/C_f] \times 100\%, \quad (1)$$

where C_0 and C_f represent the initial and final concentrations of the cations (mg L^{-1}), respectively. The distribution coefficient (K_d) was calculated using the following formula:

$$K_d = [(C_0 - C_f)/C_f]V/m, \quad (2)$$

where V represents the volume of the solution (ml) and m denotes the mass of adsorbent (g).

The concentration of TMD nanosheets was determined by digesting the sample in a mixture of HNO_3 and H_2O_2 solution, followed by testing the concentration of soluble Mo/W/Ta/Ti species via ICP-OES[7]. These batch experiments were conducted at room temperature to assess adsorption capacity, selectivity, and kinetic processes. To evaluate adsorption capacity, various concentrations of Pb^{2+} ranging from 2 to 80 mg L^{-1} were individually introduced into the TMD nanosheets solution. After 12 h of continuous stirring, the residual Pb^{2+} concentrations were quantified using ICP-MS. In order to investigate the kinetics of the Pb^{2+} adsorption process, a mixture of TMD with Pb^{2+} at a concentration of 2 mg L^{-1} was stirred for varying durations: 1, 2, 4, 8, 16, 30, and 60 min, respectively. Subsequently, the remaining Pb^{2+} concentration was promptly determined using ICP-MS after separating the Pb^{2+} adsorbed TMD nanosheets.

Filtration of Pb^{2+} through MoS_2 membrane

The filtration experiment involving Pb^{2+} through the MoS_2 membrane was conducted at room temperature using a pressure cell (Sterlitech) with an internal volume of 300 ml. To initiate the experiment, a MoS_2 membrane (1 cm in diameter) was loaded into the cell's chamber, which was then filled with Pb^{2+} solutions of varying concentrations (1 mg L^{-1} and 0.25 mg L^{-1}). The filtration experiments were initiated by applying a pressure of 1 bar using compressed N_2. Subsequently, 10 mL samples of the filtrate were periodically collected and subjected to analysis using ICP-MS. To regenerate the TMD membrane after the Pb^{2+} filtration, it was thoroughly flushed with an EDTA solution to remove the adsorbed Pb^{2+} from the membrane. This regenerated membrane was then ready for use in subsequent filtration experiments.

Material characterization

SEM (Thermo Scientific Quattro S, operated at 20 kV), TEM (Tecnai G2 spirit Twin, accelerating voltage of 120 kV), STEM (collected on a double Cs-corrected JEOL-ARM300 at 80 kV), XPS (Thermo Scientific K-Alpha Nexsa, Al Kα source gun, the binding energy was calibrated via the C1*s* peak at 284.8 eV), XAS (Beijing Synchrotron Radiation Facility, beamline 4B9A, transmission mode), Raman (WITEC 300R Raman system, 532 nm), XRD (D2 PHASER XE-T, Cu Kα radiation source, 30 kV voltage and 10 mA current), AFM (Dimension 3100, Veeco, CA), Zeta potential (Malvern Zetasizer Nano series), ICP-OES (Optima 8000 spectrometer). ICP-MS (PE Nexion 2000) was used for detecting the concentration of cation with µg L^{-1} level).

Calculation setup

In this work, the removal efficiency of Pb^{2+} on TMD materials is explored using DFT calculations with CASTEP version 7.0[44], embedded in Material Studio 7.0 (released in 2014). In particular, we have used the generalized gradient approximation (GGA) with Perdew-Burke-Ernzerhof (PBE) functionals to indicate the exchange-correlation interactions[45–47]. Meanwhile, the cutoff energy has been set to 440 eV with the ultrafine quality settings and the ultrasoft pseudopotentials are considered for all the elements. During the energy minimization processes, we have applied the k-point setting to coarse quality based on the Broyden-Fletcher-Goldfarb-Shanno (BFGS) algorithm[48]. For the TMD surfaces, we have cleaved the (001) surfaces from single layer 1T′-MoS_2, 1T′-WS_2, 1T-TaS_2, and 1T-TiS_2 in a $6 \times 6 \times 1$ supercell. To achieve accurate geometry optimizations, the following stringent convergency criteria have been applied for geometry optimizations, where the Hellmann-Feynman forces should not exceed 0.001 eV/Å, and the total energy difference should not be over 5×10^{-5} eV/atom. The calculation of the adsorption energy (E_{ad}) follows the equation:

$$E_{ad} = E_{TMD+Metal} - E_{TMD} - E_{Metal} \quad (3)$$

In the above equation, $E_{TMD+Metal}$ represents the total energy of metal ions adsorbed on TMD surfaces, E_{TMD} and E_{Metal} are the total energy of the TMD and metals.

Data availability

The authors declare that all data supporting this work are contained in graphics displayed in the main manuscript or in the Supplementary Information. Data used to generate these figures are available from the authors upon request. Source data are provided with this paper.

References

1. Zuo, K. C. et al. Electrified water treatment: fundamentals and roles of electrode materials. *Nat. Rev. Mater* **8**, 472–490 (2023).
2. Xie, X. Q. et al. Microstructure and surface control of MXene films for water purification. *Nat. Sustain.* **2**, 856–862 (2019).
3. Vörösmarty, C. J. et al. Global threats to human water security and river biodiversity. *Nature* **467**, 555–561 (2010).
4. Li, B. Y. et al. Mercury nano-trap for effective and efficient removal of mercury(II) from aqueous solution. *Nat. Commun.* **5**, 5537 (2014).
5. Peng, Y. G. et al. A versatile MOF-based trap for heavy metal ion capture and dispersion. *Nat. Commun.* **9**, 187 (2018).
6. Wang, T. C. et al. Novel Cu(II)-EDTA decomplexation by discharge plasma oxidation and coupled Cu removal by alkaline precipitation: underneath mechanisms. *Environ. Sci. Tech.* **52**, 7884–7891 (2018).
7. Dean, J. G. et al. Removing heavy metals from waste water. *Environ. Sci. Tech.* **6**, 518–522 (1972).
8. Mier, M. V. et al. Heavy metal removal with Mexican clinoptilolite: multi-component ionic exchange. *Water Res.* **35**, 373–378 (2001).
9. Wang, Z. Y. et al. Superselective removal of lead from water by two-dimensional MoS_2 nanosheets and layer-stacked membranes. *Environ. Sci. Tech.* **54**, 12602–12611 (2020).
10. Ries, L. et al. Enhanced sieving from exfoliated MoS_2 membranes via covalent functionalization. *Nat. Mater.* **18**, 1112–1117 (2019).
11. Wang, W. S. et al. High-surface-area functionalized nanolaminated membranes for energy-efficient nanofiltration and desalination in forward osmosis. *Nat. Water* **1**, 187–197 (2023).
12. World Health Organization. *Guidelines for Drinking-Water Quality* (World Health Organization, 2002).
13. Sun, Q. et al. Postsynthetically modified covalent organic frameworks for efficient and effective mercury removal. *J. Am. Chem. Soc.* **139**, 2786–2793 (2017).
14. Aguila, B. et al. Efficient mercury capture using functionalized porous organic polymer. *Adv. Mater.* **29**, 1700665 (2017).

15. Peng, Q. M. et al. Unique lead adsorption behavior of activated hydroxyl group in two-dimensional titanium carbide. *J. Am. Chem. Soc.* **136**, 4113–4116 (2014).
16. Liu, F. et al. Nanosheet-structured boron nitride spheres with a versatile adsorption capacity for water cleaning. *ACS Appl. Mater. Interfaces* **7**, 1824–1832 (2015).
17. Madadrang, C. J. et al. Adsorption behavior of EDTA-graphene oxide for Pb (II) removal. *ACS Appl. Mater. Interfaces* **4**, 1186–1193 (2012).
18. Li, W. et al. Flowerlike WSe_2 and WS_2 microspheres: one-pot synthesis, formation mechanism and application in heavy metal ion sequestration. *Chem. Commun.* **52**, 4481–4484 (2016).
19. Kumar, N. et al. Achieving controllable MoS_2 nanostructures with increased interlayer spacing for efficient removal of Pb(II) from aquatic systems. *ACS Appl. Mater. Interfaces* **11**, 19141–19155 (2019).
20. Ai, K. L. et al. MoS_2 nanosheets with widened interlayer spacing for high-efficiency removal of mercury in aquatic systems. *Adv. Funct. Mater.* **26**, 5542–5549 (2016).
21. Luo, J. M. et al. Phase-mediated heavy metal adsorption from aqueous solutions using two-dimensional layered MoS_2. *ACS Appl. Mater. Interfaces* **11**, 38789–38797 (2019).
22. Han, Q. et al. Tuning phase compositions of MoS_2 nanomaterials for enhanced heavy metal removal: performance and mechanism. *Phys. Chem. Chem. Phys.* **24**, 13305–13316 (2022).
23. Qiu, S. J. et al. Designing a 3D-MoS_2 nanocomposite based on the Donnan membrane effect for superselective Pb(II) removal from water. *Chem. Eng. J.* **452**, 139101 (2023).
24. Yang, R. J. et al. High-yield production of mono- or few-layer transition metal dichalcogenide nanosheets by an electrochemical lithium ion intercalation-based exfoliation method. *Nat. Protoc.* **17**, 358–377 (2022).
25. Zeng, Z. Y. et al. Single-layer semiconducting nanosheets: high-yield preparation and device fabrication. *Angew. Chem. Int. Ed.* **50**, 11093–11097 (2011).
26. Heising, J. et al. Exfoliated and restacked MoS_2 and WS_2: ionic or neutral species? Encapsulation and ordering of hard electropositive cations. *J. Am. Chem. Soc.* **121**, 11720–11732 (1999).
27. Xie, S. L. et al. Ultra-high-efficiency capture of lead ions over acetylenic bond-rich graphdiyne adsorbent in aqueous solution. *Proc. Natl. Acad. Sci. USA* **120**, e2221002120 (2023).
28. Zeng, Z. Y. et al. Growth of noble metal nanoparticles on single-layer TiS_2 and TaS_2 nanosheets for hydrogen evolution reaction. *Energy Environ. Sci.* **7**, 797–803 (2014).
29. Huang, X. et al. Solution-phase epitaxial growth of noble metal nanostructures on dispersible single-layer molybdenum disulfide nanosheets. *Nat. Commun.* **4**, 1444 (2013).
30. Lee, B. H. et al. Reversible and cooperative photoactivation of single-atom Cu/TiO_2 photocatalysts. *Nat. Mater.* **18**, 620–626 (2019).
31. Han, L. L. et al. A single-atom library for guided monometallic and concentration-complex multimetallic designs. *Nat. Mater.* **21**, 681–688 (2022).
32. Xu, M. Q. et al. Single-atom vibrational spectroscopy with chemical-bonding sensitivity. *Nat. Mater.* **22**, 612–618 (2023).
33. Chen, Y. et al. Phase engineering of nanomaterials. *Nat. Rev. Chem.* **4**, 243–256 (2020).
34. Yu, Y. F. et al. High phase-purity 1T'-MoS_2- and 1T'-$MoSe_2$- layered crystals. *Nat. Chem.* **10**, 638–643 (2018).
35. Lai, Z. C. et al. Metastable 1T′-phase group VIB transition metal dichalcogenide crystals. *Nat. Mater.* **20**, 1113–1120 (2021).
36. Zhao, X. X. et al. Engineering covalently bonded 2D layered materials by self-intercalation. *Nature* **581**, 171–177 (2020).
37. Zhang, J. Q. et al. Single platinum atoms immobilized on an MXene as an efficient catalyst for the hydrogen evolution reaction. *Nat. Catal.* **1**, 985–992 (2018).
38. Wu, Z.-Y. et al. A general synthesis of single atom catalysts with controllable atomic and mesoporous structures. *Nat. Synth.* **1**, 658–667 (2022).
39. Xia, C. et al. General synthesis of single-atom catalysts with high metal loading using graphene quantum dots. *Nat. Chem.* **13**, 887–894 (2021).
40. Jiao, J. Q. et al. Copper atom-pair catalyst anchored on alloy nanowires for selective and efficient electrochemical reduction of CO_2. *Nat. Chem.* **11**, 222–228 (2019).
41. Shannon, M. A. et al. Science and technology for water purification in the coming decades. *Nature* **452**, 301–310 (2008).
42. Wang, Z. Y. et al. Understanding the aqueous stability and filtration capability of MoS_2 membranes. *Nano Lett.* **17**, 7289–7298 (2017).
43. Mei, L. et al. Simultaneous electrochemical exfoliation and covalent functionalization of MoS_2 membrane for ion sieving. *Adv. Mater.* **34**, 2201416 (2022).
44. Clark, S. J. et al. First principles methods using CASTEP. *Z. Kristallog.* **220**, 567–570 (2005).
45. Perdew, J. P. et al. Generalized gradient approximation made simple. *Phys. Rev. Lett.* **77**, 3865–3868 (1996).
46. Hasnip, P. J. et al. Electronic energy minimisation with ultrasoft pseudopotentials. *Comput. Phys. Commun.* **174**, 24–29 (2006).
47. Perdew, J. P. et al. Atoms, molecules, solids, and surfaces: applications of the generalized gradient approximation for exchange and correlation. *Phys. Rev. B.* **46**, 6671–6687 (1992).
48. Head, J. D. et al. A Broyden—Fletcher—Goldfarb—Shanno optimization procedure for molecular geometries. *Chem. Phys. Lett.* **122**, 264–270 (1985).

Acknowledgements

Z.Y.Z. thanks the Young Collaborative Research Grant [Project No. C1003-23Y] and General Research Fund (GRF) [Project No. CityU11308923] support from the Research Grants Council of the Hong Kong Special Administrative Region, China, the Basic Research Project from Shenzhen Science and Technology Innovation Committee in Shenzhen, China [No. JCYJ20210324134012034], and the Applied Research Grant of City University of Hong Kong (project no. of 9667247) and Chow Sang Sang Group Research Fund of City University of Hong Kong (project no. of 9229123). Z.Y.Z. also thanks the funding supported by the Seed Collaborative Research Fund Scheme of State Key Laboratory of Marine Pollution which receives regular research funding from Innovation and Technology Commission (ITC) of the Hong Kong SAR Government. However, any opinions, findings, conclusions or recommendations expressed in this publication do not reflect the views of the Hong Kong SAR Government or the ITC. L.G. thanks the funding support from National Natural Science Foundation of China (52250402, 51991344, 52025025).

Author contributions

Z.Y.Z. proposed the research direction and supervised the project. L.M. designed and performed the experiments. M.Z.S. and B.L.H. conducted the density functional theory calculation. Y.Q.Z., Y.F.Z., J.F. and X.C.Z. helped to analyze and discuss the calculated results. Z.Z., Q.H.Z., Y.Z. and L.G. performed the scanning transmission electron microscopy characterization. L.Z. and Y.C. carried out the transmission electron microscopy characterization. J.Z., M.Y.L., W.J.Z., H.S.S., C.Y.T., and D.V. helped to discuss the experimental results. L.M., M.Z.S., R.J.Y., B.L.H. and Z.Y.Z. co-wrote the manuscript. All authors checked the manuscript and agreed with its content.

Competing interests

The authors declare no competing interests.

Additional information

Supplementary information The online version contains supplementary material available at https://doi.org/10.1038/s41467-024-52078-y.

Correspondence and requests for materials should be addressed to Bolong Huang, Lin Gu or Zhiyuan Zeng.

Peer review information *Nature Communications* thanks Xiangsheng Han and the other, anonymous, reviewer for their contribution to the peer review of this work. A peer review file is available.

[1]Department of Materials Science and Engineering, and State Key Laboratory of Marine Pollution, and Center of Super-Diamond and Advanced Films, City University of Hong Kong, Hong Kong SAR, China. [2]Department of Applied Biology and Chemical Technology, The Hong Kong Polytechnic University, Hung Hom, Kowloon, Hong Kong SAR, China. [3]Department of Chemistry, The Chinese University of Hong Kong, Hong Kong, China. [4]Beijing National Laboratory for Condensed Matter Physics, Institute of Physics, Chinese Academy of Sciences, 100190 Beijing, China. [5]School of Materials Science and Engineering, Hunan Provincial Key Laboratory of Electronic Packaging and Advanced Functional Materials, Central South University, Changsha 410083 Hunan, PR China. [6]Department of Applied Physics, Research Institute for Smart Energy, The Hong Kong Polytechnic University, Hong Kong, China. [7]State Key Laboratory of Marine Pollution and Department of Chemistry, City University of Hong Kong, 999077, Tat Chee Avenue, Kowloon, Hong Kong SAR 999077, China. [8]Center for 2D Quantum Heterostructures, Institute for Basic Science, Sungkyunkwan University (SKKU), Suwon 16419, Republic of Korea. [9]Department of Energy Science, Sungkyunkwan University (SKKU), Suwon 16419, Republic of Korea. [10]Department of Civil Engineering, The University of Hong Kong, Hong Kong SAR, China. [11]Beijing National Center for Electron Microscopy and Laboratory of Advanced Materials, Department of Materials Science and Engineering, Tsinghua University, 100084 Beijing, China. [12]Institut Européen des Membranes, IEM, UMR 5635, Université Montpellier, ENSCM, CNRS, 34000 Montpellier, France. [13]Shenzhen Research Institute, City University of Hong Kong, Shenzhen 518057, China. [14]These authors contributed equally: Liang Mei, Mingzi Sun, Ruijie Yang. ✉e-mail: bhuang@polyu.edu.hk; lingu@tsinghua.edu.cn; zhiyzeng@cityu.edu.hk